Spatially-Resolved Mid-Infrared Spectral Evidence of Space Weathering

Kainen L. Utt[1,1], Ryan C. Ogliore[1,1], Hans A. Bechtel[2,2], Jeffrey Gillis-Davis[3,3], and Bradley L. Jolliff[4,4]

[1]Laboratory for Space Sciences, Department of Physics, Washington University in St. Louis
[2]Advanced Light Source Division, Lawrence Berkeley National Laboratory
[3]Washington University, St. Louis
[4]Dept. Earth and Planetary Sciences

November 30, 2022

Abstract

Space weathering processes induce changes to the physical, chemical, and optical properties of space-exposed soil grains. For the Moon, space weathering causes reddening, darkening, and diminished contrast in reflectance spectra over visible and near-infrared wavelengths. The physical and chemical changes responsible for these optical effects occur on scales below the diffraction limit of traditional far-field spectroscopic techniques. Recently developed super-resolution spectroscopic techniques provide an opportunity to understand better the optical effects of space weathering on the sub-micrometer length scale. This paper uses synchrotron infrared nanospectroscopy to examine depth-profile samples from two mature lunar soils in the mid-infrared, 1500–700 cm-1 (6.7–14.3 μm). Our findings are broadly consistent with prior bulk observations and theoretical models of space weathered spectra of lunar materials. These results provide a direct spatial link between the physical/chemical changes in space-exposed grain surfaces and spectral changes of space-weathered bodies.

1

Detecting Sub-Micron Space Weathering Effects in Lunar Grains with Synchrotron Infrared Nanospectroscopy

K. L. Utt[1], R. C. Ogliore[1], H. A.Bechtel[2], J. J. Gillis-Davis[1], and B. L. Jolliff[3,4]

[1]Department of Physics, Washington University in St. Louis, St. Louis, MO, USA
[2]Advanced Light Source Division, Lawrence Berkeley National Laboratory, Berkeley, CA, USA
[3]Department of Earth and Planetary Sciences, Washington University in St. Louis, St. Louis, MO, USA
[4]McDonnell Center for the Space Sciences, Washington University in St. Louis, St. Louis, MO, USA

Key Points:

- Lunar soils were studied with spatially-resolved near-field spectroscopy in the mid-infrared
- Spectral effects of space weathering were observed to vary continuously over a depth of 500 nm
- Direct experimental evidence supports a connection between microstructural/chemical changes and mid-infrared effects in weathered lunar soil

Corresponding author: Kainen L. Utt, `k.l.utt@wustl.edu`

Abstract

Space weathering processes induce changes to the physical, chemical, and optical properties of space-exposed soil grains. For the Moon, space weathering causes reddening, darkening, and diminished contrast in reflectance spectra over visible and near-infrared wavelengths. The physical and chemical changes responsible for these optical effects occur on scales below the diffraction limit of traditional far-field spectroscopic techniques. Recently developed super-resolution spectroscopic techniques provide an opportunity to understand better the optical effects of space weathering on the sub-micrometer length scale. This paper uses synchrotron infrared nanospectroscopy to examine depth-profile samples from two mature lunar soils in the mid-infrared, 1500–$700\,\mathrm{cm}^{-1}$ (6.7–$14.3\,\mathrm{\mu m}$). Our findings are broadly consistent with prior bulk observations and theoretical models of space weathered spectra of lunar materials. These results provide a direct spatial link between the physical/chemical changes in space-exposed grain surfaces and spectral changes of space-weathered bodies.

Plain Language Summary

The Moon's surface, unprotected from the space environment, is bombarded with solar wind ions and micrometeoroids. These interactions are part of a process known as space weathering, which changes the physical and optical properties of lunar soils and asteroid surfaces on a microscopic scale. Technological hurdles have hindered our understanding of the connection between the physical changes caused by space weathering and the optical properties thought to result from them. Using synchrotron infrared nanospectroscopy, we examined how various weathering processes affect the infrared spectral characteristics of lunar soil grains. With these insights, we can develop better space weathering models to predict how different surfaces may be affected. The data from this investigation can also be used to calibrate laboratory analog studies of space weathering and help interpret observations of bodies similar to the Moon.

1 Introduction

The Moon is subject to frequent micrometeoroid impacts and bombardment by energetic solar wind ions. The compositional and structural changes induced by these processes on the Moon and other airless bodies are collectively referred to as space weathering (Hapke, 2001; Pieters et al., 1993). In aggregate, these changes to the morphology, chemical composition, and crystal structure of individual regolith grains alter the optical properties of the bulk soil — relative to freshly exposed lunar regolith, reflectance spectra of space exposed soils have reddened, darkened continua, and weaker diagnostic absorption peaks in the visible to infrared (IR) wavelengths. These effects have also been observed in studies of S-type asteroidal surface soils (Noguchi et al., 2011, 2014) and simulated space weathering experiments (Thompson et al., 2019; Kaluna et al., 2017; Lantz et al., 2017).

The effects of space weathering occur on a spatial scale comparable to the wavelength of visible light, presenting a unique challenge to our understanding of how various weathering processes evolve and interact to produce optical changes. The physical changes induced by space weathering, including the production of nano-phase iron particles and damage to the soil's crystal structure (i.e., amorphization), have been found to occur predominantly within 100–$200\,\mathrm{nm}$ of the grain surface (Pieters et al., 1993, 2000; Taylor et al., 2001; Noble et al., 2005). Hence, electron microscopy techniques are well-suited to characterize microstructural and micro-compositional changes. For instance, transmission electron microscopy (TEM) of weathered lunar soils has demonstrated that many of the optical changes seen in weathered soil are associated with the presence of nano-phase iron (npFe^0) particles in amorphous rims coating mineral grains (Keller & McKay, 1993, 1997; Taylor et al., 2001, 2010), and micro-phase iron that occurs in ag-

glutinates (Basu, 2005). In particular, npFe^0 grains smaller than 40 nm in diameter cause spectral reddening and darkening, while larger iron particles cause only darkening (Noble et al., 2007; Lucey & Riner, 2011). Although the physical and chemical changes caused by space weathering can be detected via TEM, the localized optical effects of these changes cannot be directly interrogated using diffraction-limited spectroscopic techniques. Traditional diffraction-limited spectroscopic techniques cannot spatially resolve features much smaller than the wavelength of light used—most npFe^0 is <40 nm in diameter. Until recently, computational modeling was required to determine the cumulative effects of space weathering on the optical properties of lunar soil (Hapke, 2001; Lucey & Riner, 2011; Lucey & Noble, 2008; Wohlfarth et al., 2019).

To bridge the gap between the optical effects of space weathering and the nanoscale physio-chemical phenomena that produce them, we used Synchrotron Infrared Nano Spectroscopy (SINS) to collect IR spectral data with sub-micrometer spatial resolution from depth-profile samples of space-exposed lunar soil. This technique is capable of ~20 nm spatial resolution, making it possible to assess the optical effects of weathering phenomena at a spatial resolution sufficient to resolve sub-micrometer products of lunar space weathering (Bechtel et al., 2014). Near-field infrared spectroscopy has previously been employed to analyze other extraterrestrial or planetary materials, including the Murchison meteorite (CM2) (Kebukawa et al., 2010), a grain (Iris) from comet 81P/Wild 2 (Dominguez et al., 2014), and the Didim meteorite (H3-5) (Yesiltas et al., 2020). This paper presents near-field infrared spectroscopic evidence of space-weathering-induced changes to mature lunar soils' optical properties in the 'fingerprint region' of the mid-infrared (1500–700 cm^{-1}; 6.7–14.3 μm).

2 Materials and Methods

2.1 Sample Preparation

The examined samples were selected from fine-grained portions of lunar soils 79221 and 10084, shown in Figures 1 and 2. The degree of surface exposure (maturity) of lunar soils is typically indicated by the ferromagnetic resonance (FMR) surface exposure index, given as FMR intensity divided by iron content (I_s/FeO) —see Morris (1976) for more detail. By this metric, both 79221 and 10084 are highly mature soils with I_s/FeO values of 81 and 78, respectively (Rhodes & Blanchard, 1982; Taylor et al., 2001). To prepare the soils for sectioning, we secured a portion of each sample to an aluminum stub with carbon tape. We subsequently coated both sample and stub with ~10 nm of gold-palladium. The coated grains were imaged in secondary and back-scattered electrons using a Tescan Mira3 field-emission scanning electron microscope (FEG-SEM). An EDAX energy-dispersive X-ray (EDX) spectrometer on the SEM was used for elemental analyses and mineral identification.

As described in greater detail below, SINS utilizes an atomic force microscope (AFM) tip to enhance near-field resonances at a sample surface. To interrogate spectral response changes as a function of depth, we created depth-profile lift-outs from the grains identified via SEM-EDX. Qualitative markers of space exposure (e.g., surface blistering, micrometeoroid impact craters, melt splash) were used to inform the site-selection for targeted liftout extraction. Lift-outs (initial thickness ≈ 1 μm) were extracted from space-exposed regions of the target grains with an FEI Quanta 3D focused ion beam (FIB) equipped with a computer-controlled Omniprobe micro-manipulator. These samples were transferred to an Omniprobe lift-out grid, upon which they were thinned to a thickness of 300–600 nm. Each sample was subsequently polished with a low-energy (5 kV, 48 pA) Ga$^+$ beam for roughly two minutes per side to remove any surface damage created during the thinning procedure (Kato, 2004). The thinned lift-outs were then placed onto an ultra-flat (surface roughness < 0.5 nm) Si chip.
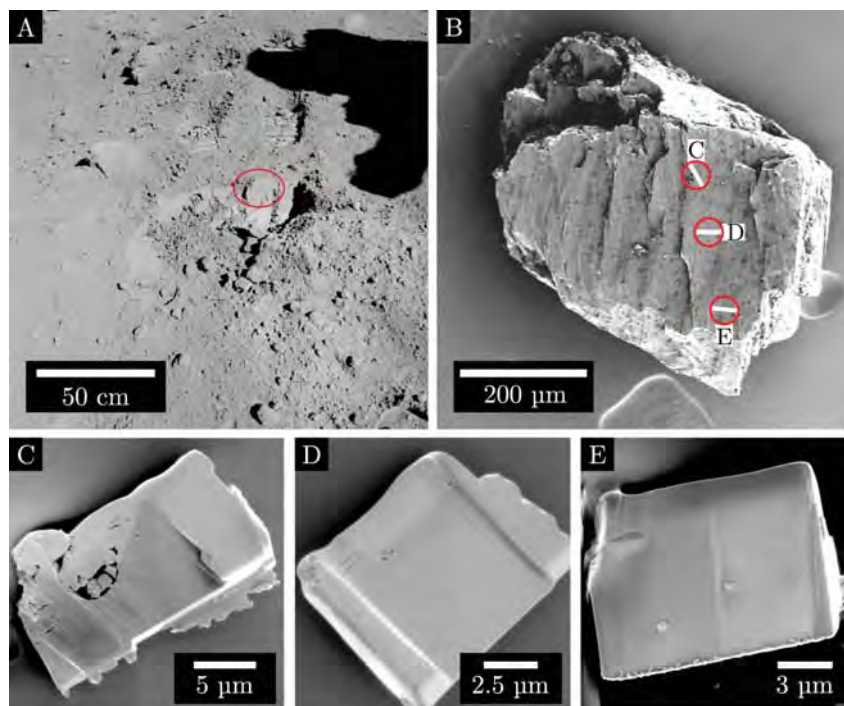
Figure 1. The geospatial context for lunar soil 79221 (Samples 1–3). **(A)** NASA photograph AS17-142-21827 showing approximate in situ sample location (circled) as recorded at the time of collection. **(B)** 2 kV SE image of host grain for samples 1–3, extracted from the circled areas. The encircled white rectangles indicate the orientation of each sample. **(C)**–**(E)** 2 kV SE images of samples 1–3, respectively, on Si substrate after thinning and low-voltage polishing.

Table 1. SEM-EDX compositions of the studied lunar samples.

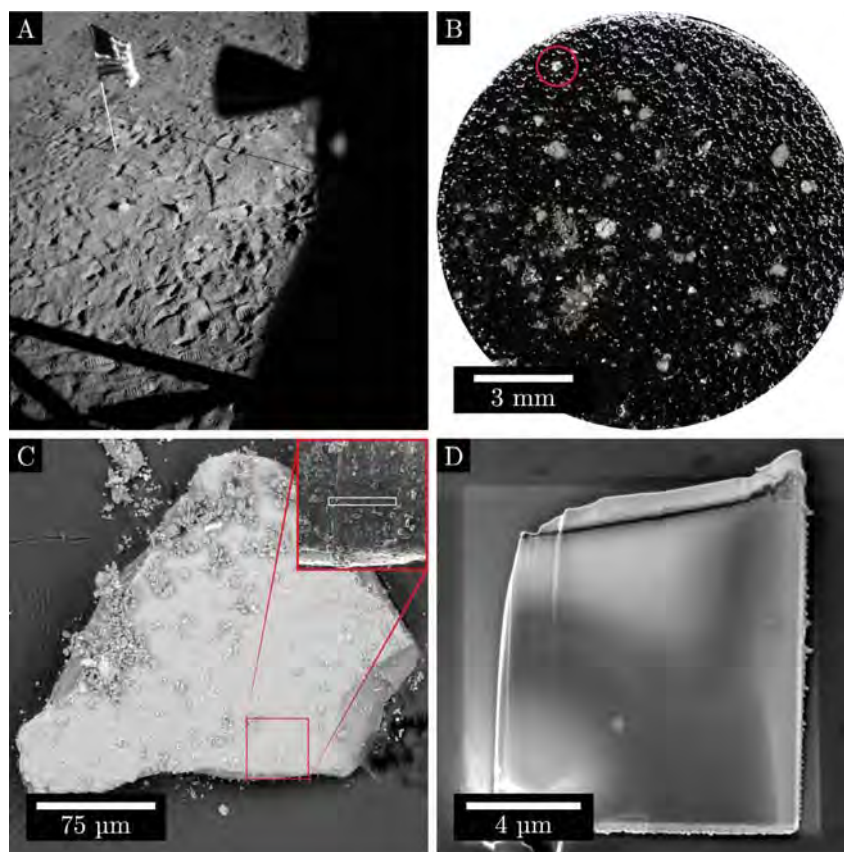| Sample	Composition (atomic percent)						
	O	Mg	Al	Si	Ca	Ti	Fe
1–3	60%	—	16%	16%	8%	—	—
4	57%	6%	5%	17%	4%	3%	7%

Figure 2. **(A)** In situ sample location of lunar soil 10084 (sample 4) as recorded from the Apollo 11 lunar module. **(B)** Optical micrograph of grains from 10084 affixed to an SEM stub with carbon tape. Sample 4 was extracted from the circled grain. **(C)** Back-scattered electron (BSE) image (15 kV) of the target grain for sample 4 with higher-magnification secondary electron (SE) image inset. The white rectangle featured in the inset image denotes the FIB extraction site for sample 4. **(D)** 2 kV SE image of sample 4 on Si substrate after thinning and low- kV polishing by FIB.
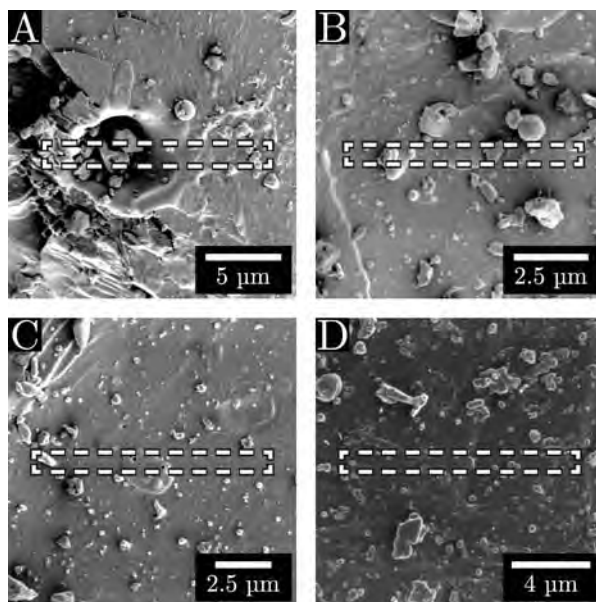
Figure 3. Close-up SE images (2 kV) of the selected FIB extraction sites shown in Figure 1B and Figure 2C. A dashed rectangle indicates the location from which each sample was extracted. **(A)** Hypervelocity micrometeoroid impact crater sampled by sample 1 (79221). **(B)** The site selected for sample 2 (79221); displays evidence of surface blistering and includes two melt splash droplets. The left droplet contains vesiculated textures. **(C)** The extraction site for sample 3 (79221) includes a vesiculated melt-splash droplet. The surface of this region of the grain displays a lesser degree of blistering than at the extraction site for sample 2. **(D)** FIB extraction site for sample 4 (10084), selected to include small melt splash droplets and mild surface blistering and amorphization.

Samples 1–3 were taken from a ~250 μm grain of 79221 with a composition consistent with anorthite-rich plagioclase (see Table 1). Sample 4 was extracted from a ~150 μm grain of 10084 with a composition consistent with Ti-, Al-rich augite, in agreement with prior studies of this sample and other Apollo 11 lunar rock samples (Ross et al., 1970). A fifth sample was taken from a terrestrial anorthite standard (Miyake Island, Japan). The studied samples and their characteristics are outlined in Table 2.

Table 2.   Descriptions of studied samples

Sample	Soil	Composition	Description
1	79221	An-rich Plagioclase	Micrometeoroid impact crater
2	79221	An-rich Plagioclase	Melt-splash coated
3	79221	An-rich Plagioclase	Surface blistering
4	10084	Ti-, Al-rich Augite	Mildly amorphized surface
—	—	Anorthite	Terrestrial mineral standard

2.2 Experimental Methods

Near-field IR spectra were collected using SINS at Beamline 5.4 at the Advanced Light Source (Bechtel et al., 2014). This technique can be thought of as a combination of Fourier-transform infrared spectroscopy (FTIR), scattering-type scanning optical microscopic (s-SNOM) techniques, and atomic force microscopy (AFM). Synchrotron IR light is coupled into an asymmetric Michelson interferometer consisting of a beamsplitter (KBr), a moving mirror (Nicolet 6700 FTIR spectrometer), and an AFM (Bruker Innova). Light is focused onto an oscillating AFM tip in one arm of the interferometer. The light scattered by the tip is combined with light reflecting off the moving mirror in the interferometer's second arm. The resulting interference signal is detected on a mercury cadmium telluride (HgCdTe) detector. With this experimental setup, the spatial resolution is determined by the radius of curvature of the AFM tip used (25 nm in this case) and is independent of the wavelength of the incident light.

The data presented in this work were collected over a broad range of mid-infrared wavenumbers, 5000–700 cm^{-1} (2.0–14.3 μm), with a spectral resolution of 8 cm^{-1}. At shorter wavelengths, however, the signal is dominated by noise caused by reduced tip-sample coupling. This high-frequency noise precludes the identification of any C-H or O-H stretch features in the sample spectra. As such, this work focuses primarily on the "fingerprint" region, 1500–700 cm^{-1} (6.7–14.3 μm). This range captures key features in the infrared spectra of both plagioclase and pyroxene while maximizing the signal-to-noise ratio. Of particular interest to lunar and remote-sensing applications, the explored spectral range encompasses the Christiansen feature —an important diagnostic feature in mid-infrared silicate spectra. Canonically, the CF is defined as an emissivity maximum associated with the frequency at which the real part of the effective dielectric constant (index of refraction) approaches unity (Christiansen, 1884). Since this condition occurs at wavelengths just short of the fundamental modes, the CF contains valuable information about silicate mineral composition (Salisbury et al., 1997; Conel, 1969).

To differentiate the near-field signal from the far-field (scattered) background, signals are detected at higher harmonics of the tip oscillation frequency, which arise from the non-linear near-field response. Here, we use the second harmonic response as a compromise between background suppression and signal-to-noise ratio. After demodulation, the interferometric signal is Fourier transformed to yield the complex near-field spectra. To first-order approximation, the spectral amplitude, $|A(\tilde{\nu})|$, is related to the real-valued component of the material's complex dielectric function (i.e., the reflection coefficient)

157 and the spectral phase, $\Phi(\tilde{\nu})$, is similarly related to the imaginary component of the di-
158 electric function (i.e., the absorption coefficient) (Xu et al., 2012; Govyadinov et al., 2014).
159 However, this approximation may not be strictly valid due to the thickness of the sam-
160 ples studied, the presence of nanoscale heterogeneities therein, and variable oscillator strengths.
161 Spectral features may therefore be shifted compared to conventional FTIR measurements
162 (Mastel et al., 2015).

163 We collected a series of line scans oriented perpendicular to the space-exposed sur-
164 face (vertically) to interrogate the effects of space weathering as a function of depth. Each
165 line scan is composed of 20–60 evenly-distributed points with an inter-point spacing of
166 20–100 nm. Three horizontally-oriented (i.e., parallel to the grain surface) scans were col-
167 lected to rule out systematic instrumental artifacts as the cause of observed depth-dependent
168 changes. Background spectra were collected before and after each line scan. The exper-
169 imental spectra were referenced to the average over relevant backgrounds. The location
170 and orientation of each line scan are shown in Figure 4 and further details can be found
171 in Table 3.

Table 3. Parameters for each line scan performed. Italic text denotes horizontally-oriented scans (i.e., parallel to the space-exposed surface). Spectra were collected with $8\,\mathrm{cm}^{-1}$ spectral resolution. At each point, a 500-scan measurement was collected over roughly six minutes. Backgrounds were collected before and after each line scan.

Sample	Scan	Length (µm)	Points	Spacing (nm)	Depth(s)	
1	1	1.70	18	95	0	− 1.70 µm
	2	1.18	22	55	0	− 1.18 µm
	3	0.89	14	65	0	− 0.89 µm
2	1	1.93	22	90	0	− 1.93 µm
	2	1.61	21	75	0	−1.61 µm
3	1	0.52	5	105	0	− 0.52 µm
	2	1.28	18	70	0.10	−1.38 µm
	3	1.28	65	20	0.34	−1.62 µm
	4	2.45	50	50	2.34	−4.79 µm
	5	0.75	11	70	30	− 750 nm
4	1	0.77	17	45	0	− 770 nm
	2	*1.45*	*29*	*50*	*4.08*	*−4.64 µm*
	3	0.80	17	45	0	− 800 nm
	4	*0.89*	*30*	*30*		*1.02 µm*
Anorthite	1	1.84	24	75	0	−1.84 µm
Standard	*2*	*1.90*	*20*	*95*		*6.35 µm*

2.3 Data Analysis

172 The data presented in this work were pre-processed using a custom program that employs commercially available fast Fourier transform software packages (Wavemetrics Igor Pro). Background and instrumental responses were removed by referencing the amplitude and phase signals to a background spectrum collected on Si or Au before and after each sample scan. The referenced amplitude and phase signals were obtained via, re-
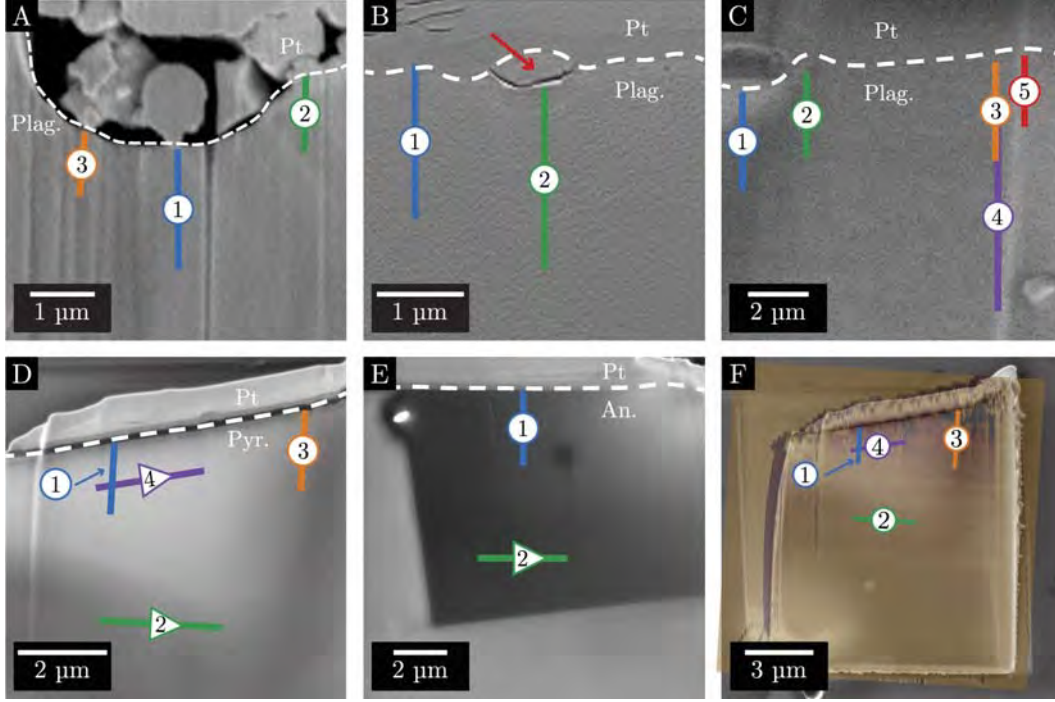
Figure 4. Close-up SE images (2 kV) of the samples shown in Figure 1C–F and Figure 2D, upon which each line scan site is superimposed. The direction of the scans oriented parallel to the space-exposed surface is indicated with an arrow. All vertically-oriented scans start in the grain interior and end near the surface. **(A)** Sample 1 (79221), scans 1–3. **(B)** Sample 2 (79221), scans 1 and 2. The second scan on this sample is located below a melt-droplet (indicated by the red arrow) that was adhered to the surface. **(C)** Sample 3 (79221), scans 1–5. The first and second scans are located below an unusually thick vesiculated melt texture. Note that scan 4 ends roughly 2.4 μm from the surface. **(D)** Sample 4 (10084), scans 1–4. The first and third scans are oriented vertically, whereas scans 2 and 4 were collected parallel to the grain surface at different depths. **(E)** Scans 1 and 2 from the terrestrial anorthite standard, respectively oriented vertically and horizontally. Note that the discoloration (the dark square in the upper right) is a temporary charging effect caused by Ga^+ ion beam use immediately prior to image capture. **(F)** An example demonstrating the alignment of the AFM topographical image (overlaid at 50% opacity) over a reference 2 kV SE image. We found general agreement in all AFM channels (i.e., tapping phase, amplitude, and topography), regarding the position of each scan and the Pt cap. However, the topographical image was used for navigation and is thus shown here.

spectively,

$$|A(\tilde{\nu})| = \frac{|A(\tilde{\nu})|_{\text{sample}}}{|A(\tilde{\nu})|_{\text{reference}}} \qquad \text{and} \qquad \Phi(\tilde{\nu}) = \Phi(\tilde{\nu})_{\text{sample}} - \Phi(\tilde{\nu})_{\text{reference}}. \qquad (1)$$

SINS amplitude spectra are generally more susceptible to topographical and instrumental artifacts than phase spectra. This susceptibility is partly because amplitude spectra typically present dispersive lineshapes, whereas phase spectra generally occur as Gaussian or Lorentzian profiles, potentially making weak features more difficult to see in amplitude data. Phase spectra have been shown to closely track the material's local absorption coefficient (Stiegler et al., 2011; Taubner et al., 2004), which is crucial for the depth-profile studies in this work. As such, we will focus primarily on phase spectra to examine the relative changes of particular spectral features as a function of depth.

The collection depth for each spectrum was calculated relative to the bottom edge of the protective Pt cap. The interface of the space-exposed surface and the Pt cap was located by overlaying high-resolution SE images (in which the Pt was visually distinct from the sample) atop the AFM topographical images used for SINS target selection. Spectra collected from the Pt cap were not used for the analyses described below. Figure 4F is an example of the alignment of topographical and SE images.

To assess the validity of the observed qualitative spectral changes over depth, we used a robust, iterative, non-linear least-squares fitting (or peak deconvolution) algorithm. Peaks in phase spectra were fit to Lorentzians with a linear baseline, following the Lorentz model for dielectrics. The constraints and initial values used for the fitting procedure were similarly physically motivated. Together, these factors improved the efficiency and likelihood of convergence for our analyses. This approach is loosely similar to the Modified Gaussian Model (MGM) developed by Sunshine, Pieters, & Pratt, 1990, with some fundamental changes implemented to account for the differences between SINS and far-field infrared spectroscopy. It should be noted that the MGM, however, is typically used with UV-visible or near infrared data. Similar fitting procedures have been used previously to analyze a suite of extraterrestrial materials such as Martian meteorites (Sunshine et al., 1993), remote sensing data from Mars (Mustard & Sunshine, 1995), and lunar soils (including the two soils studied here) (Noble et al., 2006). For a more thorough treatment of our quantitative model, please refer to the Supplementary Material.

2.4 Terrestrial Standard

For purposes of comparison, two scans were collected from a terrestrial anorthite standard. The phase spectra from these two scans are plotted in Figure 5. Spectra from the anorthite standard feature two strong absorption peaks likely corresponding to Si-O-Si asymmetric stretch Restsrahlen bands (Le Bras et al., 2003; Carmichael, 1988). The peak at approximately $1150\,\text{cm}^{-1}$ ($8.70\,\mu\text{m}$) is sharp and distinct (FWHM $\approx 60\,\text{cm}^{-1}$), whereas the peak at roughly $1035\,\text{cm}^{-1}$ ($9.66\,\mu\text{m}$) is substantially broader (FWHM $\approx 170\,\text{cm}^{-1}$) due to the presence of a shoulder roughly centered about $965\,\text{cm}^{-1}$ ($10.36\,\mu\text{m}$). These features' positions and lineshapes closely match previously reported absorption spectra for anorthite-rich plagioclase (Estep et al., 1971; Williams & Jeanloz, 1989). Given this correspondence, the shallow trough at approximately $1230\,\text{cm}^{-1}$ is likely related to the CF. Accordingly, the broad minimum centered at $\sim840\,\text{cm}^{-1}$ is likely associated with a low-phase feature between vibrational modes.

The SINS phase spectra from samples 1–3 are qualitatively similar to those from the (identically-prepared) terrestrial anorthite standard. The similarity of these spectra varies from sample to sample, as shown in Fig. 6. Spectra from samples 2 and 3 include the two major features seen in the standard (peaks at roughly $1040\,\text{cm}^{-1}$ and $1150\,\text{cm}^{-1}$), but also contain some features not observed for the terrestrial standard. By contrast, sample 1 is characterized by spectra with relatively weak and broad features, making detailed

interpretation challenging. Potential explanations for this divergence are explored further in the Discussion.

The depth-dependent spectral effects seen among samples from 79221 were not observed in spectra collected from the mineral standard, indicating that they are unlikely to have arisen due to instrumental effects (see Fig. 5). Moreover, line scans collected from the terrestrial standard at a constant depth were not found to differ significantly from those collected at variable depths, offering supporting evidence that the observed variations result from space weathering-induced microstructural and chemical changes in the uppermost layers of lunar soil grains.
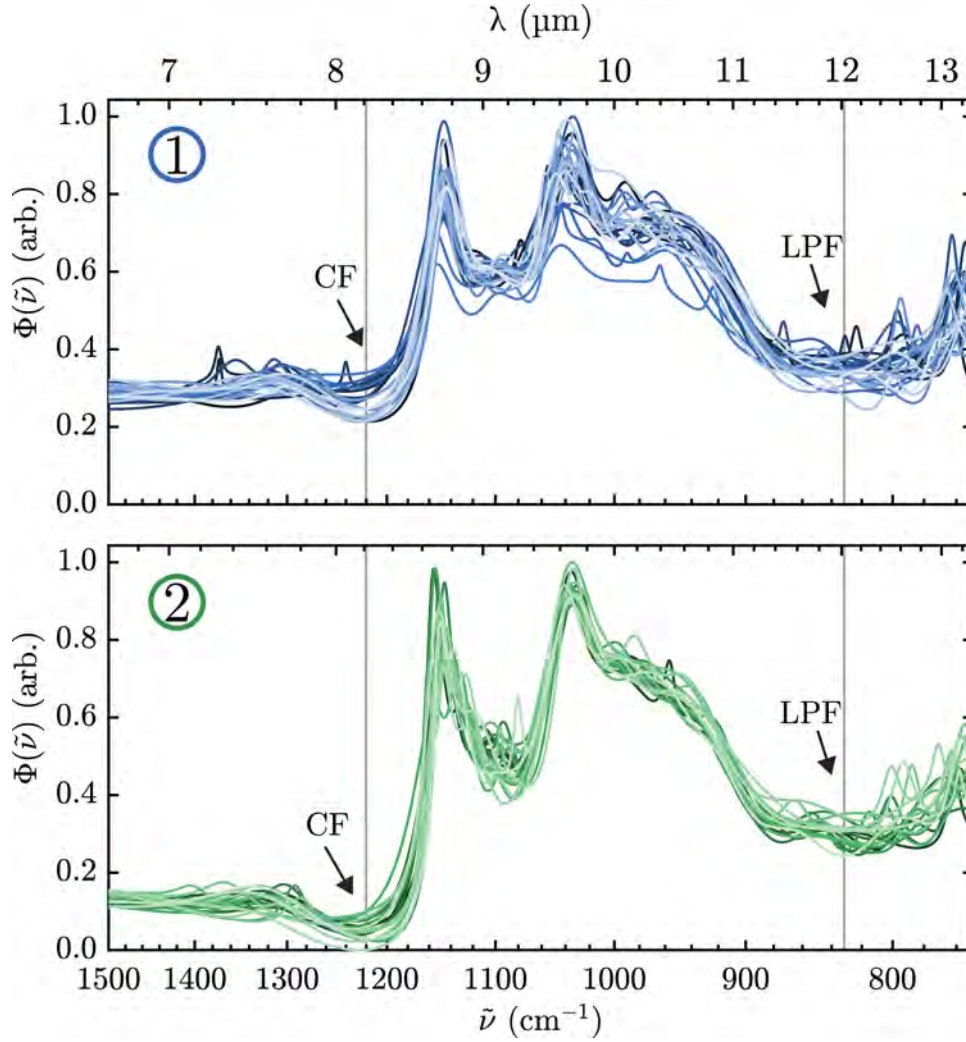

Figure 5. Line scan phase spectra collected on the terrestrial anorthite standard. Scan 1 (top panel, plotted in blue) is oriented perpendicular to the surface and starts in the grain interior. Scan 2 (bottom panel, plotted in green) is oriented parallel to the grain surface. Spectra collected at depth are plotted in darker colors, whereas the lighter colors indicate spectra collected from near the surface. The Christiansen feature (CF) and a low-phase feature (LPF) are indicated with arrows.
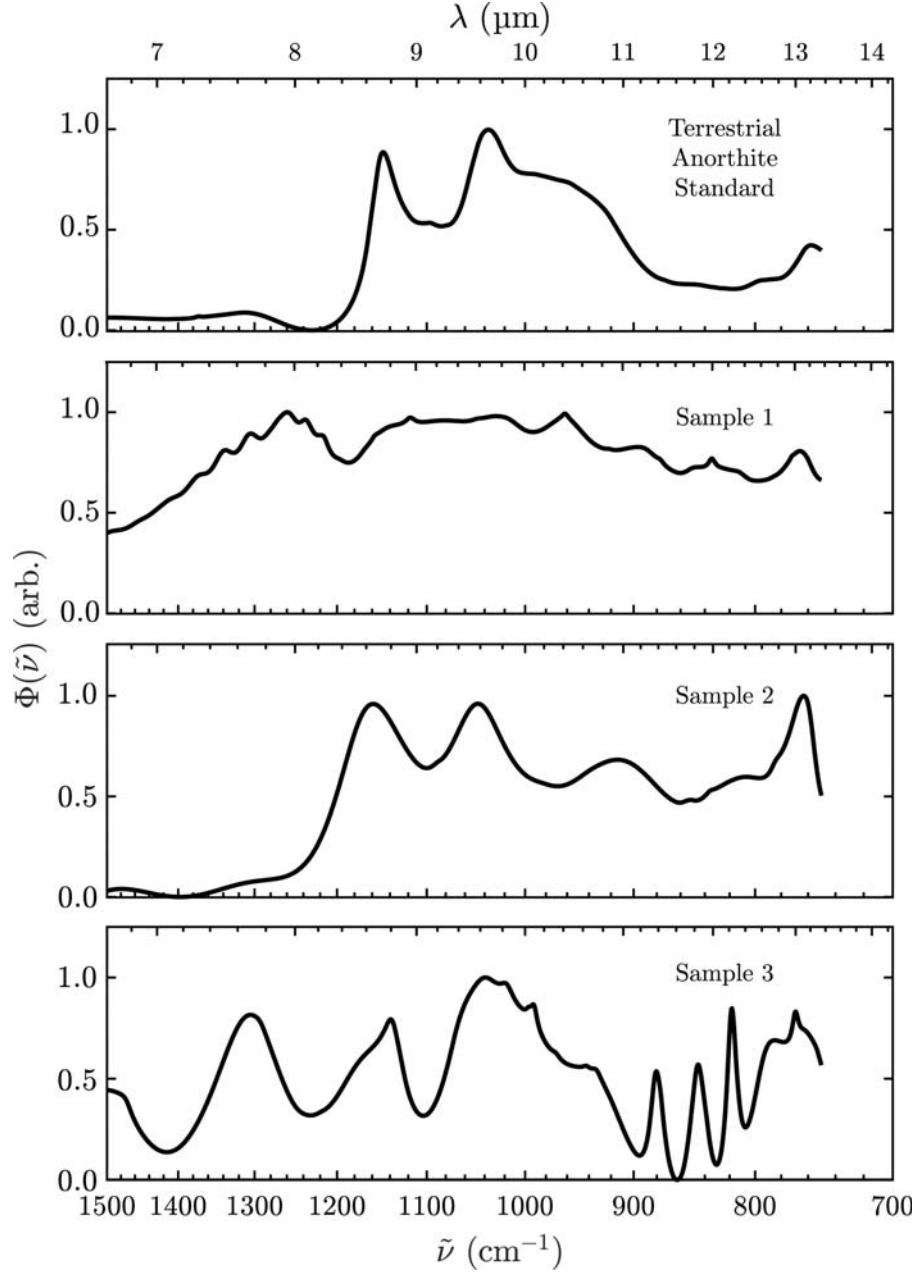
Figure 6. Comparing the average SINS phase spectra of the interiors of samples 1–3 (79221) to the terrestrial anorthite standard (Miyake, Japan). The spectra plotted for samples 1–3 are averages over the deepest portions of each line scan. The phase spectrum for the terrestrial anorthite standard is the average of all spectra from that sample.

3 Results

3.1 Micrometeoroid Impact Crater (Sample 1)

SINS phase spectra, $\Phi(\tilde{\nu})$, collected near the hypervelocity impact crater on sample 1 (see Fig. 3) exhibit systematic variations between the grain interior (far from the crater bottom) and the grain surface (just below the crater). Primary among these variations is the loss of spectral contrast with increasing proximity to the surface, as shown in Figure 7 and described below.

Two peaks in the phase spectra at $830\,\mathrm{cm}^{-1}$ ($12.05\,\mu\mathrm{m}$) and $1140\,\mathrm{cm}^{-1}$ ($8.77\,\mu\mathrm{m}$) broaden and display reduced spectral contrast with increasing proximity to the surface. These effects are most notable within $300\,\mathrm{nm}$ of the surface for both features. Near the surface, the loss of spectral contrast causes the CF to become indistinguishable from the background.
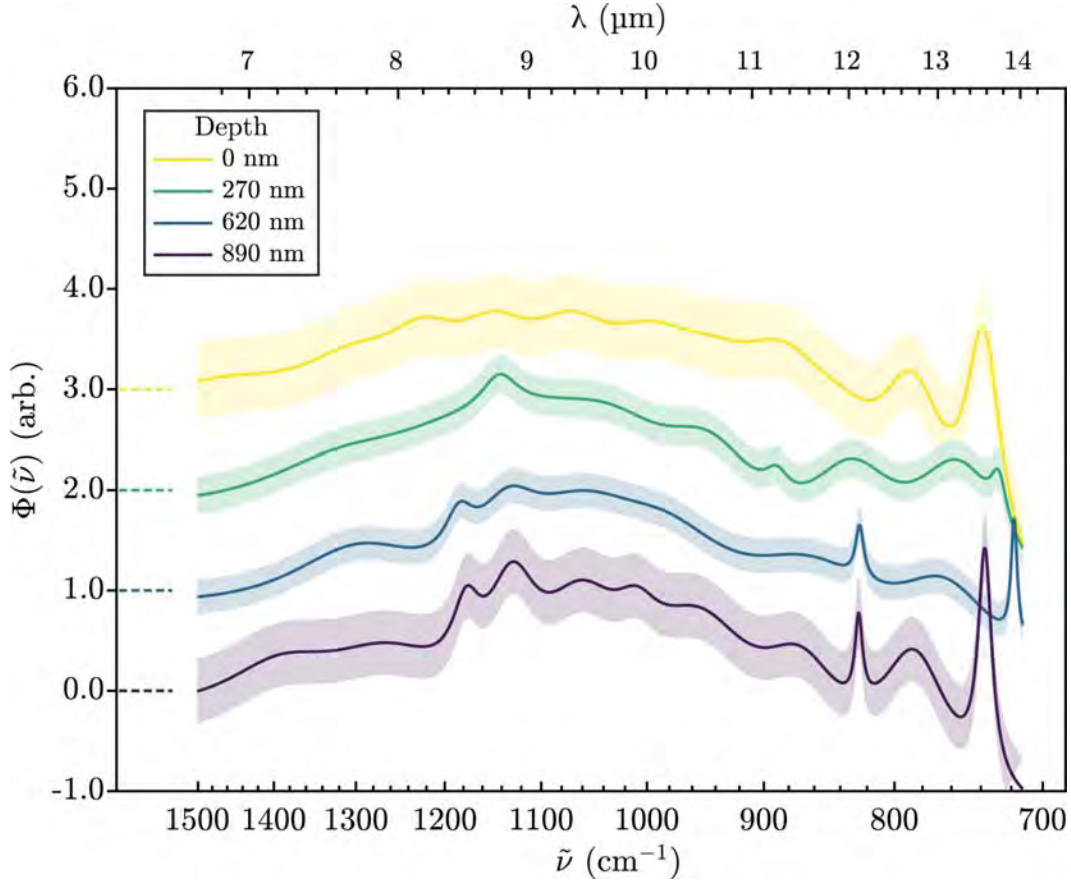

Figure 7. Computed fits of selected SINS phase spectra from scan 3 on sample 1, collected at the labeled distances from the bottom of the hypervelocity impact crater on the plagioclase grain shown in Fig. 3A and Fig. 4A. Spectra are vertically offset (dashed lines) from one another for clarity. Shaded areas indicate 2σ confidence intervals. Diminished spectral contrast was observed among spectra from close to the surface, particularly for key spectral features at $830\,\mathrm{cm}^{-1}$ ($12.05\,\mu\mathrm{m}$) and $1140\,\mathrm{cm}^{-1}$ ($8.77\,\mu\mathrm{m}$).

3.2 Melt-Splash Coating (Sample 2)

Sample 2 was collected from a melt-splash coated region approximately $150\,\mu m$ from the hypervelocity impact crater on sample 1 (see Fig. 3). The spectra from this sample are less noisy and contain sharper peaks than those described in Subsection 3.1. As shown in Figure 8, these spectra evolve as a function of depth similar to those from sample 1. We observed depth-dependent loss of spectral contrast, particularly at longer wavelengths. This effect is most prominent among spectra collected from within $400\,nm$ of the surface.

Spectra from the grain interior include several peaks in the range $\sim$950–725 cm^{-1}. At the surface, these features are difficult to distinguish from the background conclusively. The provenance of these features is explored further in the discussion. A 'reddening' baseline accompanies this trend at wavelengths $\gtrsim 11\,\mu m$, wherein the apparent slope transitions from negative to slightly positive between depths of $890\,nm$ and $400\,nm$. Two prominent peaks occur at $1045\,cm^{-1}$ $(9.6\,\mu m)$ and $1165\,cm^{-1}$ $(8.6\,\mu m)$ in spectra from all sampled depths. These features remain relatively stable over depth, with only some statistically insignificant broadening observed near the surface.
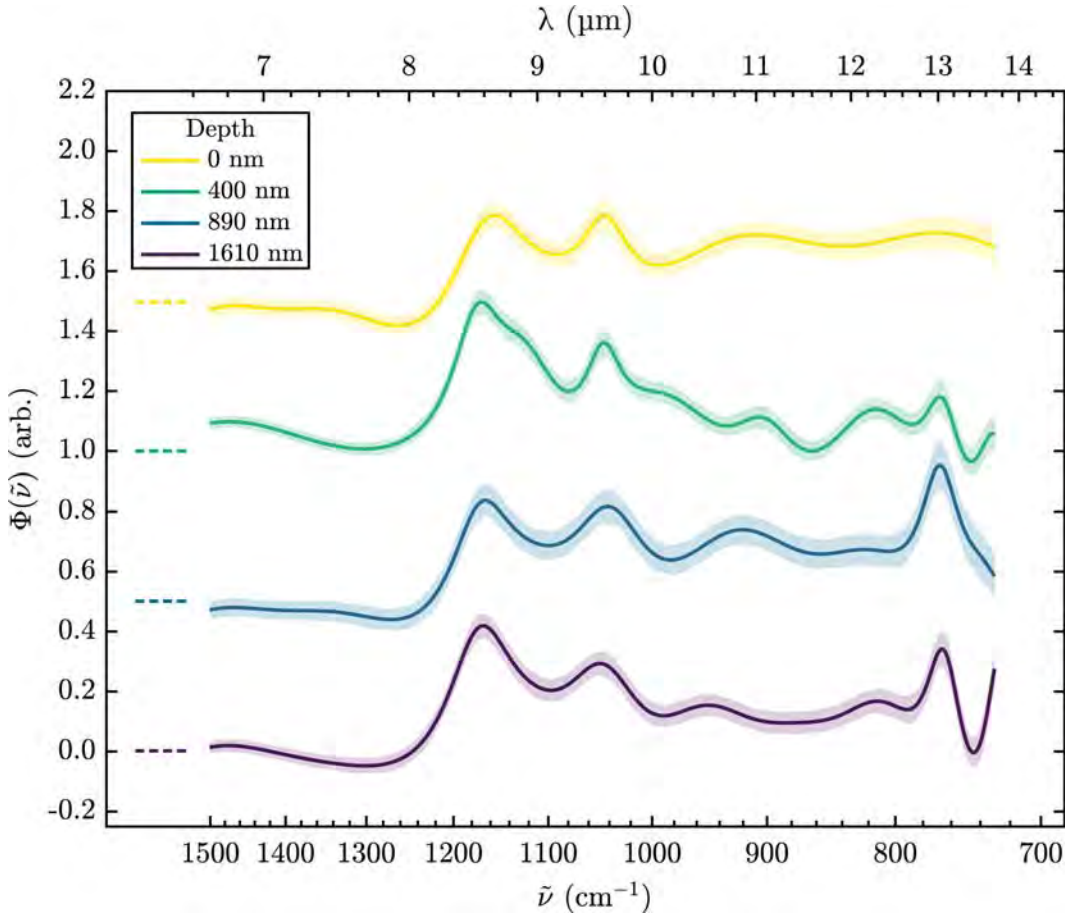

Figure 8. Computed fits of selected SINS phase spectra from scan 2 on sample 2, collected at the labeled distances from the melt-splotched surface of the plagioclase grain shown in Fig. 3B and Fig. 4B. Spectra are vertically offset (dashed lines) from one another for clarity. Shaded areas indicate 2σ confidence intervals. Diminished spectral contrast was observed close to the surface for some features. Key spectral features at $1045\,cm^{-1}$ and $1165\,cm^{-1}$ are discussed in greater detail in the text.

3.3 Surface Blistering (Sample 3)

The spectra from sample 3, characterized by its evidence of surface blistering (see Fig. 3), are shown in Figure 9. We observed depth-dependent loss of spectral contrast, particularly at wavelengths of 8.5–12 µm. This effect is most prominent among spectra collected from within 250 nm of the surface.

Importantly, this sample's spectra contain features consistent with imperfect background subtraction. In particular, the peak at $\sim$1350 cm^{-1} is consistent with some signal from the silicon substrate 'bleeding through' the sample. In contrast to the sample's diagnostic features, this peak is stronger at the surface than in the grain interior.
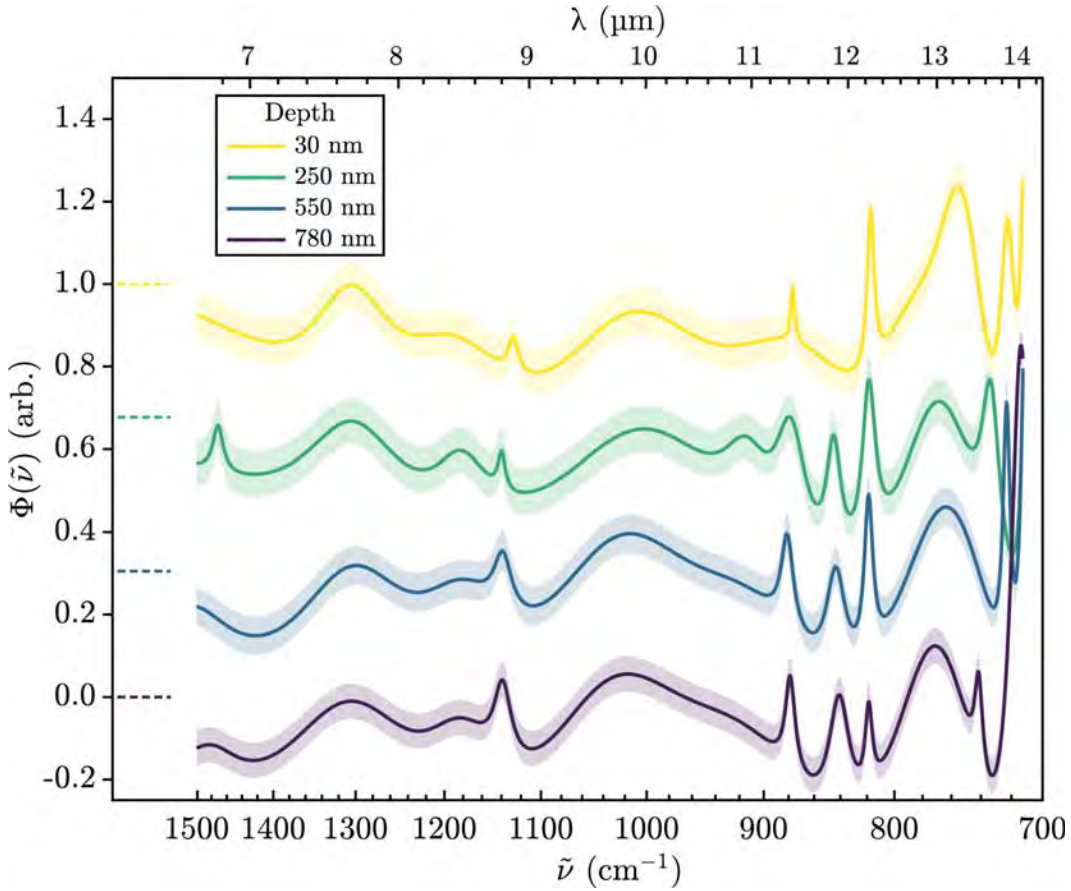

Figure 9. Computed fits of selected SINS phase spectra from scan 5 on sample 3, collected at the labeled distances from the blistered surface of the plagioclase grain shown in Fig. 3C and Fig. 4C. Spectra are vertically offset (dashed lines) from one another for clarity. Shaded areas indicate 2σ confidence intervals. Diminished spectral contrast was observed at the surface for several diagnostic features. Key spectral features at 750 cm^{-1}, 1015 cm^{-1} and 1145 cm^{-1} are discussed in greater detail in the text.

3.4 Mildly Amorphized Pyroxene (Sample 4)

As shown in Fig. 10, the spectra from sample 4 display few systematic variations over depth. Potential explanations for this are explored in the Discussion. In contrast with the spectra from samples 1–3 and the terrestrial anorthite standard, which contain several identifiable features, the spectra from this pyroxene sample are dominated by a roughly symmetric, prominent, broad peak at $1040\,cm^{-1}$ ($9.6\,\mu m$). Although this peak's intensity remains roughly constant at all depths, its width increases slightly at the surface. At depths greater than $550\,nm$, there appears to be a weak feature at $\sim\!750\,cm^{-1}$ ($13.3\,\mu m$) that broadens near the surface. However, this feature should be interpreted with caution given the variability of these spectra at low wavenumbers (long wavelengths).
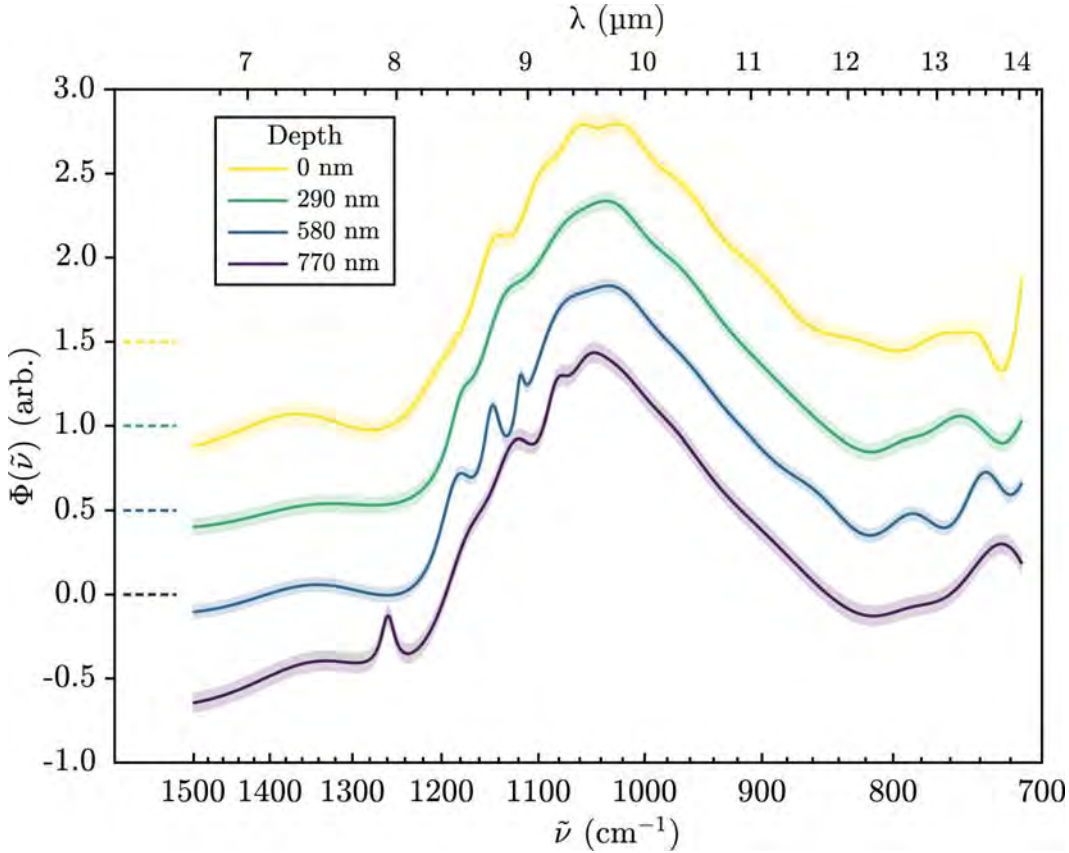

Figure 10. Computed fits of selected SINS phase spectra from scan 1 on sample 4 at a range of depths from the blistered surface (see Fig. 3D). Spectra are vertically offset (dashed lines) from one another for clarity. Shaded areas indicate 2σ confidence intervals. Spectral features were not observed to undergo substantial changes over depth, as discussed in greater detail within the text.

3.5 Depth-Dependent Spectral Effects

The collected data for samples 2 and 3 indicate that the total scattered intensity and spectral contrast are inversely correlated with distance from the space-exposed surface. Peaks present in SINS amplitude spectra from close to the surface of these two samples are significantly less distinguishable from the continuum than in spectra collected

from the crystalline grain interior (see, e.g., Fig. 8). Figure 11 illustrates this effect centered about a peak at $1145\,cm^{-1}$ found in the phase spectra of sample 3. In scans from sample 2, peaks at higher wavenumbers were more effectively suppressed than those at lower wavenumbers. Whether this trend extends to samples 1 and 4 remains unclear.
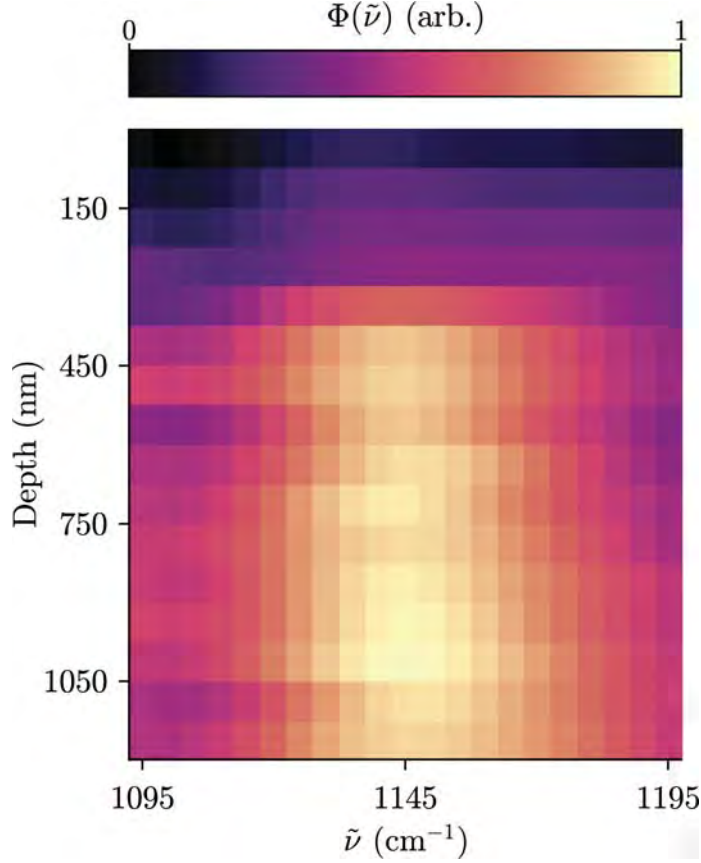

Figure 11. Color-map demonstrating the observed relationship between spectral contrast and surface proximity for the peak at roughly $1150\,cm^{-1}$ in SINS phase spectra from sample 3 (see Fig. 9 and Fig. 4E). The data for each of the five scans shown in Fig. 4C were binned by depth (16 bins,75 nm per bin) and wavenumber (20 bins, $5\,cm^{-1}$ per bin). The pixel color corresponds to the average value of the continuum-removed $\Phi(\tilde{\nu})$ spectra from the five line scans on sample 3, for the corresponding wavenumbers and depths. The effect size is markedly greater within the uppermost 300 nm of the sample, consistent with surface-correlated weathering phenomena

.

The integrated amplitude response, analogous to total scattered intensity, was observed to evolve over depth (see Figure 12). This quantity was calculated for each collected spectrum by integrating the amplitude signal over the wavenumbers of interest ($\nu \in [700\,cm^{-1}\ 2000\,cm^{-1}]$). In scans from samples 1–3, the total scattered intensity is strongly correlated with depth (i.e., spectra from close to the space-exposed surface are darker than those from within the grain interior). This darkening effect occurs in samples 1–3 over depths of 0–2000 nm. In samples 2 and 3, darkening is most pronounced in the uppermost 500 nm. Interestingly, the darkening in spectra from near the impact crater (sample 1) occurs at a shallower slope than the other 79221 samples.

294   Data from sample 4 do not display a strong correlation between scattered inten-
295 sity and depth.

4 Discussion

297   Many minerals have qualitatively different near-field and far-field IR spectra. Though
298 the two spectra may share some features, there is generally no one-to-one correlation (Hermann
299 et al., 2014; Huth et al., 2012; Pollard et al., 2015). This disparity means that we can-
300 not definitively link spectral features observed in our samples to particular vibrational
301 modes without further analysis. Despite this, many of the features we observed in our
302 samples' SINS spectra are consistent with the characteristic absorption features reported
303 in the literature.

304   The $\sim$830 cm^{-1} feature observed with varying prominence in samples 1–3 appear
305 to be related to the Si-O-Si or Al-O symmetric stretch features. Although prior work mod-
306 eling the optical constants of labradorite has not found a similar peak at roughly 830 cm^{-1}
307 (12.05 µm) in spectra of the complex coefficient (Ye et al., 2019), these peaks are present
308 in a majority of the spectra from samples 1–3 and appear to follow a depth-dependent
309 trend similar to other peaks. Similar features have additionally been reported in mid-
310 infrared absorption spectra of anorthite and albite (Dorschner, 1971). That this feature
311 is more pronounced for these samples result from the presence of the hypervelocity im-
312 pact crater on the host grain for samples 1–3 and the high Al-content relative to other
313 plagioclase minerals. Al-O$_4$ tetrahedra are more susceptible to deformation under pres-
314 sure than their Si-O$_4$ counterparts (Johnson et al., 2003; Williams & Jeanloz, 1989; Williams,
315 1998). It has been speculated that (Si, Al)-O$_4$ tetrahedra are susceptible to metastable
316 'defects' under pressure that lead to, for example, Si-O-Si links between adjacent tetra-
317 hedra that may alter the stretch and bending vibrational modes (Santamaria-Perez et
318 al., 2016). Alternatively, it is hypothetically possible that these peaks could be an indi-
319 cation of silanol (Si-O-H) that formed formed on the surface of the sample or on the sub-
320 strate underneath the sample. Since the spectra were normalized to an average of stan-
321 dard spectra, which included scans collected on the Si-chip or nearby platinum cap, this
322 scenario is highly unlikely.

323   Both soils 79221 and 10084 are classified as mature, with FMR maturity indices
324 of I_s/FeO = 81 and 75, respectively (Morris, 1978). However, the maturity index is by
325 definition a bulk property of soils. As such, the individual grains that comprise a ma-
326 ture soil are likely to have various exposure ages. Although sample 4 displays far less pro-
327 nounced space weathering effects than samples 1–3, this is more likely to be a reflection
328 of the different mineral chemistry.

329   Previous studies on experimentally shocked feldspars have shown that absorption
330 bands weaken and broaden due to increasing glass content, particularly at shock pres-
331 sures above $\sim$20 GPa (Nash et al., 1993; Johnson et al., 2002, 2003). In contrast, pyrox-
332 enes are more resilient to increasing shock pressures. Studies show little change in spec-
333 tral properties with shock pressures of 45 GPa and up to 65 GPa (Adams et al., 1979;
334 Johnson et al., 2002).

335   Shock effects may also be responsible for the apparent dissimilarity between spec-
336 tra from sample 1 and those from the anorthite standard. The region directly below the
337 micrometeoroid impact crater (on sample 1) experienced much greater pressures than
338 the material in samples 2 and 3. The most prominent feature at roughly 1100 cm^{-1} in
339 phase spectra from sample 1 may result from a shock-induced spectral broadening of the
340 1000 cm^{-1} and 1150 cm^{-1} features seen for samples 2–3 and the terrestrial anorthite stan-
341 dard. These differences could alternatively be explained by the presence of compositional
342 or structural inhomogeneities in the soil grain. Should this interpretation be correct, our
343 observations serve to reinforce the value of SINS for spectroscopic investigation of micrometer-
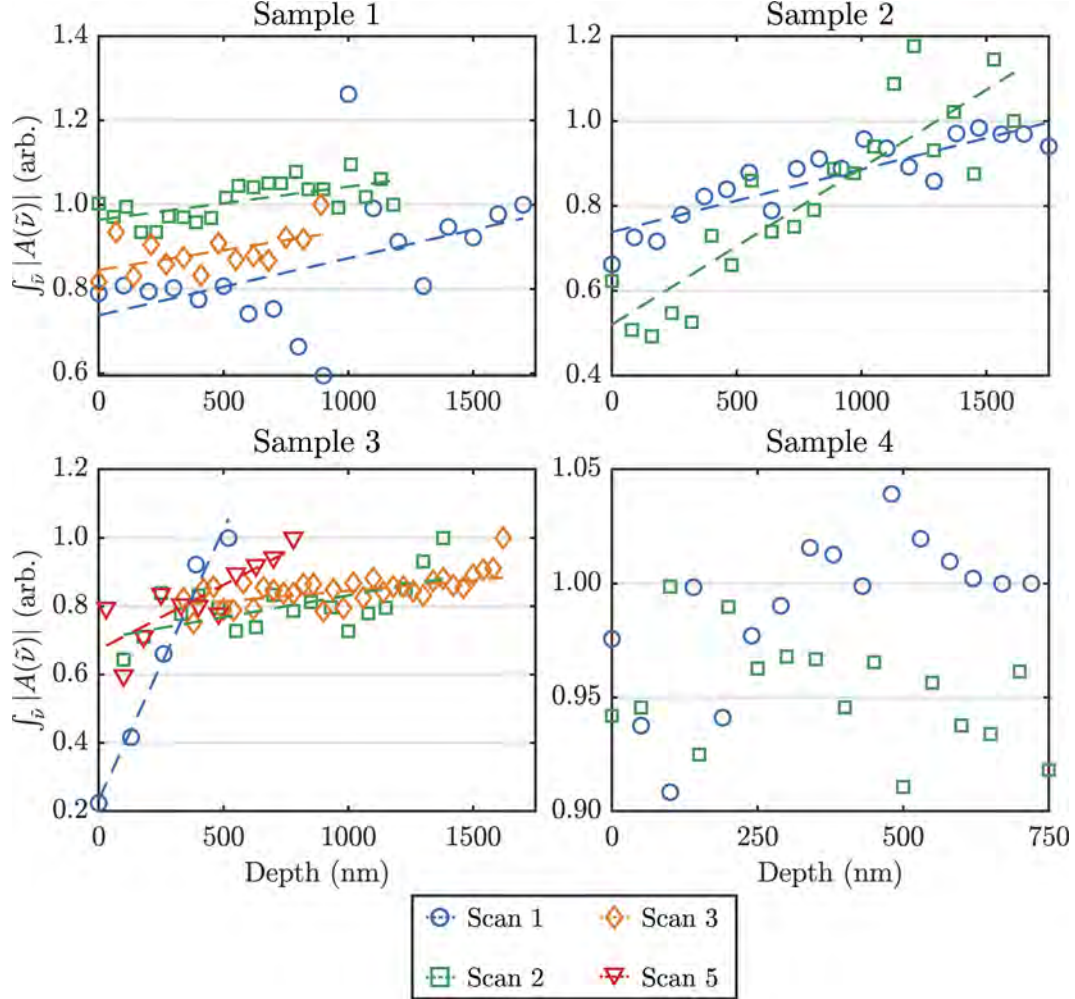
Figure 12. The amplitude response for each collected spectrum, integrated over the range $\nu \in [700\,\mathrm{cm}^{-1}, 2000\,\mathrm{cm}^{-1}]$. This integrated amplitude response (or total scattered intensity, related to the reflectivity coefficient) is plotted as a function of distance from the space-exposed surface. Each scan is plotted using the same color scheme as in Figure 4. (Note: the shallowest point of scan 4 from sample 3 is beyond $2\,\mu\mathrm{m}$. As such, it is omitted from this figure.) Darkening occurs with greater proximity to the space-exposed surface in samples 2 and 3. Sample 1, which samples a hypervelocity impact crater on the same anorthite-rich plagioclase grain as samples 2 and 3, displays a shallower darkening trend than the other samples from 79221. There does not appear to be a strong correlation between depth and integrated amplitude response for sample 4. The dashed lines plotted for sections 1–3 are simple linear fits meant only to guide the eye.

scale mineralogical variations. The signal produced by diffraction-limited techniques is an average over various mineral structures or compositions, making it unlikely that such minor deviations in chemical composition would be detectable.

In samples 2 and 3, we observed reduced total scattered intensity with increasing proximity to the space exposed surface (see Fig. 12). This darkening may be associated with an increasing concentration of $npFe^0$ near the surface (Noble et al., 2007; Lucey & Riner, 2011). Surface-correlated amorphization may be a more parsimonious explanation, however, since the host grain for samples 1–3 does not contain an appreciable amount of iron. Suppose that the observed darkening results from the amorphous surface layers produced by long-term exposure to the space environment. In that case, it is plausible that the hypervelocity impact (sample 1) vaporized or melted this layer; this could explain why no darkening was observed for sample 1 despite originating from the same soil grain as samples 2 and 3. This scenario is consistent with the widespread evidence of impact-induced shock and vitrification seen near the crater in sample 1 (see Fig. 7). Similarly, we did not observe a robust correlation between total scattered intensity and depth for sample 4, suggesting that it contains limited concentrations of $npFe^0$ or is otherwise more robust to the space environment over the studied wavelength range.

However, it is important to note that samples 2 and 3 were extracted parallel to one another and nearly perpendicular to section 1. As such, the effect of crystallographic orientation cannot be ruled out when comparing results among the samples. The primary observations —namely, that there is depth-dependent spectral variation between the grain interior and the space-exposed surface —are not affected by this limitation.

Where present, the darkening effect is most apparent within 500 nm of the grain surface (see Fig. 12). This depth falls just outside of the observed range of thicknesses for amorphous rims in lunar soil ($\sim$10–350 nm; Burgess and Stroud (2018); Christoffersen et al. (1996)), but well within the range of thicknesses for glassy silicate layers (10–1000 nm) thought to have been produced by micrometeoroid impacts (Noble et al., 2005). For comparison, the average implantation depth of solar wind-produced H and He has been estimated as $\sim$20–100 nm (Christoffersen et al., 1996; Farrell et al., 2015; Tucker et al., 2019).

That we observed space weathering effects at depths greater than the penetration range of typical solar wind protons could suggest that the implanted hydrogen diffused into the grain. Although some diffusion undoubtedly occurs, it is unlikely to be the dominant cause of the observed effects given the relatively poor H-retention of lunar soil (Farrell et al., 2015). Alternatively, the effects observed could result from the occasional bombardment of the lunar surface by solar energetic particles (SEPs), which are substantially more energetic than solar wind ions. Hydrogen SEPs have kinetic energies of 2–10 MeV (Mewaldt et al., 2009), whereas typical solar wind H^+ ions have kinetic energies of $\sim$1 keV (Gosling et al., 1976). Although SEPs are likely to implant further into lunar soil than average solar wind ions, they occur far less frequently. Without additional support from independent lines of evidence (e.g., observing tracks via TEM), these confounding factors preclude definitive conclusions about the role of SEPs in the weathering of our samples.

5 Conclusions

We used SINS to examine surface-correlated, mid-IR space weathering effects in lunar soil grains. In general, our results are consistent with the spectral changes previously hypothesized to be correlated with the microstructural and compositional changes measured by TEM. Crucially, however, our results demonstrate that SINS (and related techniques) can be used to investigate the spatial scales over which ion irradiation and micrometeoroid bombardment affect the soil's optical properties. With a spatial resolution comparable to the scale of space-weathering induced microstructural and chem-

ical changes, SINS can be used to establish a direct link to bulk space weathering effects. As such, we have shown that this technique fills the gap between TEM microstructural studies and far-field FTIR measurements.

The data presented above provide clear evidence supporting previous findings that space weathering effects result from highly localized features (on the order of tens of nanometers). We found that the effect size varies continuously (at the sampled spatial resolution) over a micrometer-scale range of depths. Our results additionally indicate that soil maturity indices should be used with caution when discussing micron-scale sub-samples of lunar soil. While the soil maturity index is a reliable predictor of large-scale weathering effects, our results reinforce the variability of exposure history among a soil's constituent grains.

The techniques utilized in this study have been shown to produce results similar to those observed in bulk lunar soils. Taking advantage of techniques with spatial resolutions on the order of tens of nanometers, such as afforded by SINS, may prove useful for studying the relative contribution of each small-scale process (e.g., solar wind implantation, nano-phase iron production, micrometeoroid impacts) to the overarching space weathering phenomenon. SINS data may also inform and refine the techniques used to simulate weathering phenomena in the laboratory. With a more detailed understanding of the spectral effects of charged-particle irradiation on mineral and soil grains, it may also be possible to draw parallels to, inter alia, silicate processing in the interstellar medium (Chiar & Tielens, 2006). Detailed studies of the association between specific molecular vibrational modes and the features present in SINS spectra of minerals may shed further light on various space weathering mechanisms. Information regarding the molecular bonds affected by space weathering, paired with precise chronometry and compositional measurements of weathered lunar soils, may help to constrain or validate current models of space weathering processes.

Data Availability Statement:

The data used for this research is available at the Digital Research Material Repository at Washington University in St. Louis (Utt et al., 2020).

References

Adams, J. B., Hörz, F., & Gibbons, R. V. (1979). Effects of shock-loading on the reflectance spectra of plagioclase, pyroxene, and glass. In *Lunar and Planetary Science Conference* (Vol. 10, pp. 1–3). Retrieved from https://ui.adsabs.harvard.edu/abs/1979LPI....10....1A

Basu, A. (2005). Nanophase Fe^0 in lunar soils. *J. Earth Syst. Sci.*, *114*(3), 375–380. doi: 10.1007/BF02702956

Bechtel, H. A., Muller, E. A., Olmon, R. L., Martin, M. C., & Raschke, M. B. (2014). Ultrabroadband infrared nanospectroscopic imaging. *PNAS (USA)*, *111*(20), 7191–7196. doi: 10.1073/pnas.1400502111

Burgess, K., & Stroud, R. (2018). Phase-dependent space weathering effects and spectroscopic identification of retained helium in a lunar soil grain. *Geochimica et Cosmochimica Acta*, *224*, 64–79. doi: 10.1016/j.gca.2017.12.023

Carmichael, R. S. (1988). *Practical Handbook of Physical Properties of Rocks and Minerals (1988)*. CRC Press. doi: 10.1201/9780203710968

Chiar, J. E., & Tielens, A. G. G. M. (2006). Pixie dust: the silicate features in the diffuse interstellar medium. *ApJ*, *637*(2), 774–785. doi: 10.1086/498406

Christiansen, C. (1884). Untersuchungen über die optischen Eigenschaften von fein vertheilten Körpern. *Annalen der Physik*, *259*(10), 298–306. doi: 10.1002/andp.18842591008

Christoffersen, R., Mckay, D. S., & Keller, L. P. (1996). Microstructure, chemistry, and origin of grain rims on ilmenite from the lunar soil finest fraction. *Meteoritics & Planetary Science*, *31*(6), 835–848. doi: 10.1111/j.1945-5100.1996.tb02117.x

Conel, J. E. (1969). Infrared emissivities of silicates: Experimental results and a cloudy atmosphere model of Spectral emission from condensed particulate mediums. *Journal of Geophysical Research*, *74*(6), 1614–1634. doi: 10.1029/jb074i006p01614

Dominguez, G., Mcleod, A., Gainsforth, Z., Kelly, P., Bechtel, H. A., Keilmann, F., . . . Basov, D. (2014). Nanoscale infrared spectroscopy as a non-destructive probe of extraterrestrial samples. *Nature Communications*, *5*(1), 1–10.

Dorschner, J. (1971). Infrared spectra of silicate grains. *Astronomische Nachrichten*, *293*(1), 53. Retrieved from https://ui.adsabs.harvard.edu/abs/1971AN...293...53D doi: 10.1002/asna.19712930113

Estep, P. A., Kovach, J. J., & Karr, J., C. (1971). Infrared vibrational spectroscopic studies of minerals from Apollo 11 and Apollo 12 lunar samples. *Lunar and Planetary Science Conference Proceedings*, *2*, 2137. Retrieved from https://ui.adsabs.harvard.edu/abs/1971LPSC....2.2137E

Farrell, W. M., Hurley, D. M., & Zimmerman, M. I. (2015). Solar wind implantation into lunar regolith: hydrogen retention in a surface with defects. *Icarus*, *255*, 116–126. doi: 10.1016/j.icarus.2014.09.014

Gosling, J. T., Hildner, E., MacQueen, R. M., Munro, R. H., Poland, A. I., & Ross, C. L. (1976). The speeds of coronal mass ejection events. *Solar Physics*, *48*(2), 389–397. doi: 10.1007/bf00152004

Govyadinov, A. A., Mastel, S., Golmar, F., Chuvilin, A., Carney, P. S., & Hillenbrand, R. (2014). Recovery of permittivity and depth from near-field data as a step toward infrared nanotomography. *ACS Nano*, *8*(7), 6911–6921. doi: 10.1021/nn5016314

Hapke, B. (2001). Space weathering from Mercury to the asteroid belt. *JGR: Planets*, *106*(E5), 10039–10073. doi: 10.1029/2000je001338

Hermann, P., Hoehl, A., Ulrich, G., Fleischmann, C., Hermelink, A., Kästner, B., . . . Ulm, G. (2014). Characterization of semiconductor materials using synchrotron radiation-based near-field infrared microscopy and nano-FTIR spectroscopy. *Optics Express*, *22*(15), 17948. doi: 10.1364/oe.22.017948

Huth, F., Govyadinov, A., Amarie, S., Nuansing, W., Keilmann, F., & Hillenbrand, R. (2012). Nano-FTIR absorption spectroscopy of molecular fingerprints at 20 nm spatial resolution. *Nano Letters*, *12*(8), 3973–3978. doi: 10.1021/nl301159v

Johnson, J. R., Hörz, F., Lucey, P. G., & Christensen, P. R. (2002). Thermal infrared spectroscopy of experimentally shocked anorthosite and pyroxenite: implications for remote sensing of Mars. *Journal of Geophysical Research*, *107*(E10). doi: 10.1029/2001JE001517

Johnson, J. R., Hörz, F., & Staid, M. I. (2003). Thermal infrared spectroscopy and modeling of experimentally shocked plagioclase feldspars. *American Mineralogist*, *88*(10), 1575–1582. doi: 10.2138/am-2003-1020

Kaluna, H. M., Ishii, H. A., Bradley, J. P., Gillis-Davis, J. J., & Lucey, P. G. (2017). Simulated space weathering of Fe- and Mg-rich aqueously altered minerals using pulsed laser irradiation. *Icarus*, *292*, 245–258. doi:

10.1016/j.icarus.2016.12.028

Kato, N. I. (2004). Reducing focused ion beam damage to transmission electron microscopy samples. *Journal of electron microscopy*, *53*(5), 451–458.

Kebukawa, Y., Nakashima, S., & Zolensky, M. E. (2010). Kinetics of organic matter degradation in the Murchison meteorite for the evaluation of parent-body temperature history. *Meteoritics & Planetary Science*, *45*(1), 99–113.

Keller, L. P., & McKay, D. S. (1993). Discovery of vapor deposits in the lunar regolith. *Science*, *261*(5126), 1305–1307. doi: 10.1126/science.261.5126.1305

Keller, L. P., & McKay, D. S. (1997). The nature and origin of rims on lunar soil grains. *Geochimica et Cosmochimica Acta*, *61*(11), 2331–2341. doi: 10.1016/ S0016-7037(97)00085-9

Lantz, C., Brunetto, R., Barucci, M. A., Fornasier, S., Baklouti, D., Bourçois, J., & Godard, M. (2017). Ion irradiation of carbonaceous chondrites: a new view of space weathering on primitive asteroids. *Icarus*, *285*, 43–57. doi: 10.1016/j.icarus.2016.12.019

Le Bras, A., Erard, S., Bras, A., & Erard, S. (2003). Reflectance spectra of regolith analogs in the mid-infrared: effects of grain size. *Planetary and Space Science*, *51*(4-5), 281–294. doi: 10.1016/s0032-0633(03)00017-5

Lucey, P. G., & Noble, S. K. (2008). Experimental test of a radiative transfer model of the optical effects of space weathering. *Icarus*, *197*(1), 348–353. doi: 10 .1016/j.icarus.2008.05.008

Lucey, P. G., & Riner, M. A. (2011). The optical effects of small iron particles that darken but do not redden: evidence of intense space weathering on Mercury. *Icarus*, *212*(2), 451–462. doi: 10.1016/j.icarus.2011.01.022

Mastel, S., Govyadinov, A. A., de Oliveira, T. V. A. G., Amenabar, I., & Hillenbrand, R. (2015). Nanoscale-resolved chemical identification of thin organic films using infrared near-field spectroscopy and standard Fourier transform infrared references. *Applied Physics Letters*, *106*(2), 023113. doi: 10.1063/1.4905507

Mewaldt, R. A., Leske, R. A., Stone, E. C., Barghouty, A. F., Labrador, A. W., Cohen, C. M. S., ... Wiedenbeck, M. E. (2009). STEREO observations of energetic neutral hydrogen atoms during the 2006 December 5 solar flare. *The Astrophysical Journal*, *693*(1), L11–L15. doi: 10.1088/0004-637x/693/1/l11

Morris, R. V. (1976). Surface exposure indices of lunar soils: a comparative FMR study. *LPSC*, *1*, 315–335.

Morris, R. V. (1978). The surface exposure (maturity) of lunar soils: some concepts and I_S/FeO compilation. In *Lunar and Planetary Science Conference* (Vol. 9, pp. 2287–2297).

Mustard, J. F., & Sunshine, J. M. (1995). Seeing through the dust: martian crustal heterogeneity and links to the SNC meteorites. *Science*, *267*(5204), 1623–1626.

Nash, D. B., Salisbury, J. W., Conel, J. E., Lucey, P. G., & Christensen, P. R. (1993). Evaluation of infrared emission spectroscopy for mapping the moon's surface composition from lunar orbit. *Journal of Geophysical Research*, *98*(E12), 23535. doi: 10.1029/93je02604

Noble, S. K., Keller, L. P., & Pieters, C. M. (2005). Evidence of space weathering in regolith breccias I: lunar regolith breccias. *MAPS*, *40*(3), 397–408. doi: 10 .1111/j.1945-5100.2005.tb00390.x

Noble, S. K., Pieters, C. M., Hiroi, T., & Taylor, L. A. (2006). Using the modified gaussian model to extract quantitative data from lunar soils. *Journal of Geophysical Research: Planets*, *111*(E11). doi: 10.1029/2006JE002721

Noble, S. K., Pieters, C. M., & Keller, L. P. (2007). An experimental approach to understanding the optical effects of space weathering. *Icarus*, *192*(2), 629–642. doi: 10.1016/j.icarus.2007.07.021

Noguchi, T., Kimura, M., Hashimoto, T., Konno, M., Nakamura, T., Zolensky,

M. E., ... Ishibashi, Y. (2014). Space weathered rims found on the surfaces of the Itokawa dust particles. *Meteoritics and Planetary Science*, *49*(2), 188–214. doi: 10.1111/maps.12111

Noguchi, T., Nakamura, T., Kimura, M., Zolensky, M. E., Tanaka, M., Hashimoto, T., ... Okazaki, R. (2011). Incipient space weathering observed on the surface of Itokawa dust particles. *Science*, *333*(6046), 1121–1125. doi: 10.1126/science.1207794

Pieters, C., Fischer, E., Rode, O., & Basu, A. (1993). Optical effects of space weathering: the role of the finest fraction. *Journal of Geophysical Research*, *98*(E11), 20817. doi: 10.1029/93JE02467

Pieters, C., Taylor, L., Noble, S., Keller, L., Hapke, B., Morris, R., ... Wentworth, S. (2000). Space weathering on airless bodies: resolving a mystery with lunar samples. *MAPS*, *35*(5), 1101–1107. doi: 10.1111/j.1945-5100.2000.tb01496.x

Pollard, B., Maia, F. C. B., Raschke, M. B., & Freitas, R. O. (2015). Infrared vibrational nanospectroscopy by self-referenced interferometry. *Nano Letters*, *16*(1), 55–61. doi: 10.1021/acs.nanolett.5b02730

Rhodes, J., & Blanchard, D. (1982). Apollo 11 breccias and soils: aluminous mare basalts or multi-component mixtures? *Lunar and Planetary Science Conference*, *12*, 607–620.

Ross, M., Bence, A. E., Dwornik, E. J., Clark, J. R., & Papike, J. J. (1970). Mineralogy of the lunar clinopyroxenes, augite and pigeonite. *Geochim. Cosmochim. Acta Suppl.*, *1*, 839.

Salisbury, J. W., Basu, A., & Fischer, E. M. (1997). Thermal infrared spectra of lunar soils. *Icarus*, *130*(1), 125–139. doi: 10.1006/icar.1997.5809

Santamaria-Perez, D., Thomson, A., Segura, A., Pellicer-Torres, J., Manjon, F. J., Corà, F., ... McMillan, P. F. (2016). Metastable structural transformations and pressure-induced amorphization in natural $(Mg,Fe)_2SiO_4$ olivine under static compression: A Raman spectroscopic study. *American Mineralogist*, *101*(7), 1642–1650. doi: 10.2138/am-2016-5389ccby

Stiegler, J. M., Abate, Y., Cvitkovic, A., Romanyuk, Y. E., Huber, A. J., Leone, S. R., & Hillenbrand, R. (2011). Nanoscale infrared absorption spectroscopy of individual nanoparticles enabled by scattering-type near-field microscopy. *ACS Nano*, *5*(8), 6494–6499.

Sunshine, J. M., McFadden, L.-A., & Pieters, C. M. (1993). Reflectance spectra of the Elephant Moraine A79001 meteorite: implications for remote sensing of planetary bodies. *Icarus*, *105*(1), 79–91.

Sunshine, J. M., Pieters, C. M., & Pratt, S. F. (1990). Deconvolution of mineral absorption bands: an improved approach. *Journal of Geophysical Research: Solid Earth*, *95*(B5), 6955–6966.

Taubner, T., Hillenbrand, R., & Keilmann, F. (2004). Nanoscale polymer recognition by spectral signature in scattering infrared near-field microscopy. *Applied Physics Letters*, *85*(21), 5064–5066.

Taylor, L. A., Pieters, C., Patchen, A., Taylor, D.-H. S., Morris, R. V., Keller, L. P., & McKay, D. S. (2010). Mineralogical and chemical characterization of lunar highland soils: insights into the space weathering of soils on airless bodies. *Journal of Geophysical Research*, *115*(E2), E02002. doi: 10.1029/2009JE003427

Taylor, L. A., Pieters, C. M., Keller, L. P., Morris, R. V., & McKay, D. S. (2001). Lunar mare soils: space weathering and the major effects of surface-correlated nanophase Fe. *Journal of Geophysical Research: Planets*, *106*(E11), 27985–27999. doi: 10.1029/2000JE001402

Thompson, M. S., Loeffler, M. J., Morris, R. V., Keller, L. P., & Christoffersen, R. (2019). Spectral and chemical effects of simulated space weathering of the Murchison CM2 carbonaceous chondrite. *Icarus*, *319*, 499–511. doi: 10.1016/j.icarus.2018.09.022

Tucker, O. J., Farrell, W. M., Killen, R. M., & Hurley, D. M.   (2019).   Solar wind implantation into the lunar regolith: Monte Carlo simulations of H retention in a surface with defects and the H^2 exosphere. *Journal of Geophysical Research: Planets*, *124*(2), 278–293. doi: 10.1029/2018je005805

Utt, K. L., Ogliore, R. C., Bechtel, H. A., Gillis-Davis, J. J., & Jolliff, B. L.   (2020). *Data for 'spatially-resolved mid-infrared spectral evidence of space weathering'* (Vol. 27).   Digital Research Materials (Data & Supplemental files).   doi: 10.7936/xavh-ag19

Williams, Q. (1998). High-pressure infrared spectra of feldspars: Constraints on compressional behavior, amorphization, and diaplectic glass formation. In *Geophysical monograph series* (pp. 531–543).   American Geophysical Union.   doi: 10 .1029/gm101p0531

Williams, Q., & Jeanloz, R.   (1989).   Static amorphization of anorthite at 300K and comparison with diaplectic glass.   *Nature*, *338*(6214), 413–415.   doi: 10.1038/ 338413a0

Wohlfarth, K. S., Wöhler, C., & Grumpe, A.   (2019).   Space weathering and lunar OH/H$_2$O — insights from ab initio Mie modeling of submicroscopic iron.   *The Astronomical Journal*, *158*(2), 80. doi: 10.3847/1538-3881/ab26af

Xu, X. G., Rang, M., Craig, I. M., & Raschke, M. B.   (2012).   Pushing the sample-size limit of infrared vibrational nanospectroscopy: from monolayer toward single molecule sensitivity.   *The Journal of Physical Chemistry Letters*, *3*(13), 1836–1841. doi: 10.1021/jz300463d

Ye, C., Rucks, M. J., Arnold, J. A., & Glotch, T. D.   (2019).   Mid-infrared optical constants of labradorite, a triclinic plagioclase mineral.   *Earth and Space Science*, *6*(12), 2410–2422. doi: 10.1029/2019ea000915

Yesiltas, M., Kaya, M., Glotch, T., Brunetto, R., Maturilli, A., Helbert, J., & Ozel, M.   (2020).   Biconical reflectance, micro-Raman, and nano-FTIR spectroscopy of the Didim (H3-5) meteorite: Chemical content and molecular variations.   *Meteoritics & Planetary Science*.

Supporting Information for "Detecting Sub-Micron Space Weathering Effects in Lunar Grains with Synchrotron Infrared Nanospectroscopy"

K. L. Utt[1], R. C. Ogliore[1], H. A.Bechtel[2], J. J. Gillis-Davis[1], and

B. L. Jolliff[3,4]

[1]Department of Physics, Washington University in St. Louis, St. Louis, MO, USA

[2]Advanced Light Source Division, Lawrence Berkeley National Laboratory, Berkeley, CA, USA

[3]Department of Earth and Planetary Sciences, Washington University in St. Louis, St. Louis, MO, USA

[4]McDonnell Center for the Space Sciences, Washington University in St. Louis, St. Louis, MO, USA

Contents of this file

1. Text S1

Additional Supporting Information (Files uploaded separately)

1. Captions for Datasets S1 to S6

———

Corresponding author: Kainen L. Utt (k.l.utt@wustl.edu)

June 24, 2021, 3:00pm

Text S1. We used an iterative, non-linear, and robust peak fitting (deconvolution) procedure to determine peak parameters for SINS phase spectra. The procedure uses a trust-region minimization algorithm to fit a linear combination of Lorentzians with a local linear background (see (1)) to the data. Robustness is ensured by minimizing the residuals' summed square and using bi-square weighting to reduce the impact of outliers. The general equation for this fit is given by

$$f(\tilde{\nu}) = \left(p_1 \left(\tilde{\nu} - p_3 \right) + p_2 \right) + \sum_{i=1}^{n} \frac{a_i}{\pi} \left(\frac{c_i}{\left(b_i - \tilde{\nu} \right)^2 + c_i^2} \right), \tag{1}$$

where p_1, p_2, and p_3 are the coefficients of the local linear baseline. The remaining coefficients — a_i, b_i, and c_i — relate to the amplitude, position, and width of the relevant peak. The number of peaks (n) required to reliably produce a fit with sufficiently random residuals varied between samples. However, we found that $n = 12$ peaks was generally sufficient for stable convergence to a near-optimal solution in the lunar plagioclase samples. Fewer peaks were required to fit the spectra from the pyroxene sample.

This approach was chosen to accommodate the relatively low signal-to-noise ratio in some spectra; iterative models are more robust than classical methods when the signal is noisy (Gautam et al., 2015). To reduce the number of iterations required for the model fit to converge to a near-optimum solution, we introduced physically-motivated constraints on the coefficient values and initialized the algorithm with reasonable starting guesses for each parameter's values. These constraints are included alongside other model specifications in Data Set S3.

Note that the spectra were not smoothed before performing the fitting procedure — to do so would result in potentially severe underestimation errors when propagating uncertainties and estimating sample statistics (O'Haver, 2020).

Captions for Data Sets (Files uploaded separately)

Data Set S1. Raw SINS spectra for studied samples (sections 1–4 and the terrestrial anorthite standard). The relevant folders additionally contain the background spectral files (.CSV) that were used. These files are organized by section and scan. The original files, in proprietary .SPA format, are excluded from this Data Set due to file-size constraints. Copies of the .SPA files can be made available to interested parties upon request.

Data Set S2. This dataset is comprised of background-referenced and Fourier-transformed SINS spectra (.CSV). Note that both the amplitude and phase signals are included here. These files are organized by section and scan.

Data Set S3. The compressed folder contains the initial conditions for the iterative fitting model as well as the peak parameters calculated thereby. These data are formatted as .CSV files.

Data Set S4. The compressed folder contains 16 animated .GIF files (one for each linescan) displaying the fitted, un-renormalized phase spectra from each point in the linescan. The general darkening trend can be seen in spite of the noise.

Data Set S5. The individual frames of the animations included in Data Set S4. Files are saved in .PNG format with a name in the style of:

`\S[Sample #]_LS[Scan #]_[Depth]nm_[Phase/Amp].png`

Data Set S6. This dataset contains the fitted spectra (.CSV) and 2σ confidence intervals (CI). The files contained in this dataset are formatted such that the first column contains the wavenumbers, the second column contains the fitted spectra evaluated at that wavenumber, and the third and fourth columns contain the CI for the fit.

References

Gautam, R., Vanga, S., Ariese, F., & Umapathy, S. (2015). Review of multidimensional data processing approaches for raman and infrared spectroscopy. *EPJ Techniques and Instrumentation*, *2*(1), 1–38.

O'Haver, T. (2020). *A Pragmatic Introduction to Signal Processing*. University of Maryland at College Park. Retrieved from `https://terpconnect.umd.edu/~toh/spectrum/`